# nature communications



**Article** 

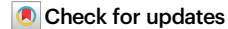
https://doi.org/10.1038/s41467-025-60472-3

# Deterministic generation of two-dimensional multi-photon cluster states

Received: 17 March 2025

Accepted: 23 May 2025

Published online: 01 July 2025



James O'Sullivan  $\mathbb{O}^{1,2,5,7} \boxtimes$ , Kevin Reuer  $\mathbb{O}^{1,2,7} \boxtimes$ , Aleksandr Grigorev<sup>1,2</sup>, Xi Dai<sup>1,2</sup>, Alonso Hernández-Antón<sup>1,2</sup>, Manuel H. Muñoz-Arias<sup>3</sup>, Christoph Hellings  $\mathbb{O}^{1,2}$ , Alexander Flasby<sup>1,2</sup>, Dante Colao Zanuz<sup>1,2</sup>, Jean-Claude Besse  $\mathbb{O}^{1,2}$ , Alexandre Blais  $\mathbb{O}^3$ , Daniel Malz  $\mathbb{O}^4$ , Christopher Eichler  $\mathbb{O}^{1,2,6}$  & Andreas Wallraff  $\mathbb{O}^{1,2}$ 

Multidimensional cluster states are a key resource for robust quantum communication, measurement-based quantum computing and quantum metrology. Here, we present a device capable of emitting large-scale entangled microwave photonic states in a two dimensional ladder structure. The device consists of a pair of coupled superconducting transmon qubits which are each tuneably coupled to a common output waveguide. This architecture permits entanglement between each transmon and a deterministically emitted photonic qubit. By interleaving two-qubit gates with controlled photon emission, we generate  $2 \times n$  grids of time- and frequency-multiplexed cluster states of itinerant microwave photons. We generate states with fidelities above 0.50 for up to eight qubits and, in addition, observe nonzero localizable entanglement for states of up to 16 qubits. We expect the device architecture to be capable of generating a wide range of other tensor network states such as tree graph states, repeater states or the ground state of the toric code, and to be readily scalable to generate larger and higher dimensional states.

Multipartite entangled states, such as cluster states, are an essential resource for quantum computation and communication<sup>1,2</sup>. Universal measurement-based quantum computing requires large-scale resource states with entanglement in at least two dimensions<sup>3,4</sup>. Cluster states consisting of a few photonic qubits entangled in two dimensions have been generated using deterministic protocols and discrete variable encoding<sup>5</sup>, but for useful applications the scale of such states must be greatly increased. Generation of large 2D cluster states on-demand and with high fidelity remains an outstanding challenge.

State generation based on the heralding of successful detection events can achieve high fidelities. However, due to the probabilistic nature of heralding methods, the success rate decreases rapidly with increasing qubit number. Deterministic protocols are therefore strongly preferred for practical applications. Cluster states have been generated deterministically in matter-based<sup>6-10</sup> and photonic systems<sup>5,11-15</sup>. Tensor network states (the class of states to which cluster states belong to) in matter-based systems<sup>7-10</sup> are limited in size by the number of available stationary qubits. One way around this limitation is to reuse qubits, either via mid-circuit reset<sup>16</sup> or by repeatedly entangling and emitting itinerant photonic qubits<sup>17,18</sup>. Emitting itinerant photonic qubits permits the generation of states consisting of far more photonic qubits than the number of available stationary qubits. Continuous-variable systems were used to generate large-scale photonic two-<sup>12,13</sup> and three-dimensional cluster states<sup>15</sup>. However, states using discrete-variable encoding in both the microwave<sup>5,19</sup> and the

<sup>1</sup>Department of Physics, ETH Zurich, Zurich, Switzerland. <sup>2</sup>Quantum Center, ETH Zurich, Zurich, Switzerland. <sup>3</sup>Institut Quantique and Département de Physique, Université de Sherbrooke, Sherbrooke, QC, Canada. <sup>4</sup>Department of Mathematical Sciences, University of Copenhagen, Copenhagen, Denmark. <sup>5</sup>Present address: CEA Paris-Saclay, Gif-sur-Yvette, France. <sup>6</sup>Present address: Physics Department, University of Erlangen-Nuremberg, Erlangen, Germany. <sup>7</sup>Those authors contributed equally, Impact O'Sullivan Kovin Payer. <sup>7</sup>Q proj. impact contributed equally. Impact O'Sullivan Kovin Payer. <sup>7</sup>Q proj. impact contributed equally.

<sup>7</sup>These authors contributed equally: James O'Sullivan, Kevin Reuer. ⊠e-mail: james.osullivan@cea.fr; kevin.reuer@phys.ethz.ch; andreas.wallraff@phys.ethz.ch

optical regime<sup>11,14</sup> were limited so far to 12 photonic qubits for 1D entanglement<sup>19,20</sup> and to 8 photonic qubits in 2D using post-selection<sup>21</sup> (4 photonic qubits without post-selection<sup>5</sup>). Therefore, deterministic generation of significantly larger multidimensional tensor network states has yet to be demonstrated.

Superconducting circuits<sup>22,23</sup> are an excellent platform for realizing devices capable of generating such multi-qubit cluster states<sup>5,19</sup>. Superconducting qubits may be engineered to couple strongly to coplanar waveguide structures<sup>24,25</sup> and tunable couplers allow for rapidly switchable interactions between circuit elements with a high on/off ratio<sup>26</sup>.

Here, we use a superconducting device to deterministically emit a two-dimensional cluster state consisting of itinerant microwave-frequency photonic qubits, further developing the devices and concepts used in ref. 19. By sequentially emitting time- and frequency multiplexed photonic qubits, we generate a  $2 \times n$  ladder-like cluster state, as illustrated in Fig. 1a. We then characterize the generated state using efficient quantum state tomography methods<sup>27,28</sup>. Our approach takes advantage of sequential emission of photonic qubits into a waveguide which can be low loss<sup>29</sup>, to reduce the required number of stationary qubits and additional potentially lossy elements such as memories<sup>30,31</sup> or delay lines<sup>5,32</sup>. This approach allows the system to emit states with a higher fidelity and consisting of significantly more qubits than the current state-of-the-art<sup>5,21</sup>.

#### Results

#### Device architecture and cluster state generation protocol

To generate ladder-like cluster states, we use two transmon qubits whose lowest three levels we label  $|g\rangle$ ,  $|e\rangle$  and  $|f\rangle$ , tunably coupled to each other<sup>33</sup>. We refer to these as 'source qubits',  $S_1$  and  $S_2$ . In addition, each source qubit is tunably coupled to a waveguide, allowing for controlled emission of photons  $P_i$ , see Fig. 1a. To generate multipartite entangled states,  $S_1$  and  $S_2$  are entangled and subsequently emit itinerant photonic qubits  $P_i$  (red and blue photon envelopes) sequentially.

The procedure is repeated many times to generate  $2 \times n$  ladder-like cluster states. We implement this scheme with a device consisting of four superconducting transmon qubits as shown in Fig. 1b. The source qubits  $S_1$  (red) and  $S_2$  (blue) are transmon qubits with fixed  $|g\rangle \leftrightarrow |e\rangle$ transition frequencies of 5.589 GHz (S<sub>1</sub>,  $T_1 = 27 \,\mu\text{s}$ ,  $T_2^* = 22 \,\mu\text{s}$ ) and 5.619 GHz ( $S_2$ ,  $T_1 = 22 \mu s$ ,  $T_2^* = 23 \mu s$ ). We realize the tunable coupling to a common waveguide for each source qubit via a frequency-tunable emitter qubit (brown, E1 at 5.754 GHz and E2 at 5.354 GHz) and a tunable coupler (orange, C1 and C2). The emitter qubits are strongly coupled to the common waveguide, such that any excitation of the emitter qubits rapidly decays into the waveguide as an itinerant photonic qubit with characteristic decay times of  $T_1 = 2/\kappa = 54$  ns (E<sub>1</sub>) and 42 ns (E<sub>2</sub>). The coupling between the source qubits is also realized by a tunable coupler, C<sub>SS</sub>. The tunable couplers consist of two parallel coplanar waveguides (CPWs) coupling two neighboring qubits 19,26,34. One CPW has a superconducting quantum interference device (SQUID) placed in the middle of the center conductor allowing fluxtuning of the CPW's inductance and thus its effective electrical length. Choosing a particular bias, we can utilize destructive interference between the fields propagating along each path to cancel the interaction between the two qubits 19,26,34. By modulating the flux threading the SQUID loop using a flux line, we parametrically drive the sideband transitions illustrated in Fig. 1c-e, enabling two-qubit gates 19,34-36.

Figure 1f shows the quantum circuit used to generate a  $2 \times n$  ladder-like cluster state<sup>18</sup>. The protocol begins with a Hadamard gate on both  $S_1$  and  $S_2$  followed by a CZ gate between these two qubits. To implement the CZ gate, we parametrically drive a  $2\pi$  rotation on the  $|ee\rangle \leftrightarrow |fg\rangle$  transition<sup>35</sup>, as illustrated in Fig. 1c. This imparts a conditional relative geometric phase between the two qubits<sup>35,37</sup>. The phase accumulated depends on the detuning of the  $|ee\rangle \leftrightarrow |fg\rangle$  pulse<sup>38</sup>—a resonant pulse results in a phase shift of  $\pi$ , thus enacting a CZ gate. The CZ gate is followed by controlled emission of a photonic qubit from  $S_1$  and  $S_2$  via CNOT gates. We perform two-qubit gates between a source qubit  $S_1$  or  $S_2$  and a photonic qubit  $P_i$  by using the emitter qubits,

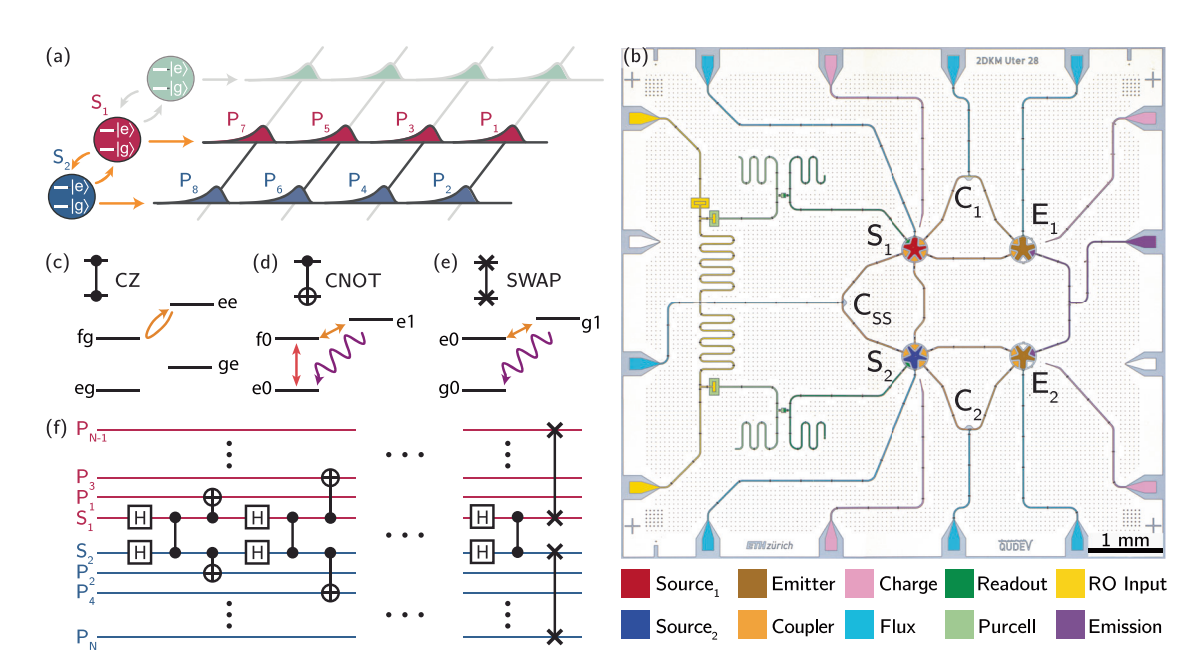


**Fig. 1** | **A source of photonic tensor-network states. a** Schematic of the entanglement and emission scheme. Couplings are depicted as orange arrows. **b** False-color micrograph of the device, consisting of source qubits  $S_1$  (red) and  $S_2$  (blue), emitter qubits  $E_1$  and  $E_2$  (brown) and tunable couplers  $C_1$ ,  $C_2$  and  $C_{SS}$  (orange). Common readout (yellow) and emission (purple) lines permit frequency-multiplexed qubit readout and photon emission. **c** Illustration of the controlled-Z gate (CZ) between two source qubits by driving the  $|ee\rangle \leftrightarrow |fg\rangle$  (orange) sideband

transition. Illustration of the physical implementation of (**d**) the controlled emission (CNOT) of a photon using a  $\pi$  pulse on the  $|e\rangle \leftrightarrow |f\rangle$  manifold (red), the  $|f0\rangle \leftrightarrow |e1\rangle$  sideband transition (orange), and the subsequent decay into the transmission line (purple), and **e** the emission of a photon via a SWAP operation using the  $|e0\rangle \leftrightarrow |g1\rangle$  sideband transition (orange). **f** Quantum circuit used to generate a  $2 \times n$  cluster state. Source qubits are denoted as  $S_1$  (red),  $S_2$  (blue), emitted photonic qubits as  $P_i$ . H denotes a Hadamard gate.

whose lowest two levels we label  $|0\rangle$  and  $|1\rangle$ . The CNOT gate, shown in Fig. 1d. is realized by first performing a  $\pi_{ef}$  rotation on the source qubit and then parametrically driving the  $|f0\rangle \leftrightarrow |e1\rangle$  transition<sup>19,36</sup>. If excited, the emitter subsequently decays into the waveguide, emitting an itinerant microwave photon<sup>25,27</sup>. A photon is only emitted if the source qubit is initially in |e|, realizing a CNOT gate between the source and the emitted photonic qubit. For the emission of the first n-1 pairs of photons a gate sequence consisting of Hadamard-CZ-CNOT is repeated n-1 times. In the last emission step, emission of the photonic qubits is done via a SWAP gate from S<sub>1</sub> to E<sub>1</sub> and from S<sub>2</sub> to E<sub>2</sub> instead of a CNOT gate. We perform such a SWAP gate by transferring the excitation into the emitter qubit by parametrically driving the  $|e0\rangle \leftrightarrow |g1\rangle$ transition<sup>19,36</sup>, as shown in Fig. 1e. These final SWAP gates disentangle S<sub>1</sub> and S2 from the generated entangled photonic state. With this protocol, in every emission step a pair of photonic qubits is generated simultaneously, i.e., their temporal modes start at the same time, but at different frequencies, resulting in a  $2 \times n$  ladder-like cluster state. Note that even though the photonic qubits' envelopes start simultaneously, the shape and duration of the envelope is different, due to the different coupling rates for  $S_1$  and  $S_2$ .

To reduce cross-talk between the source qubits, which are detuned by less than 30 MHz (due to a frequency targeting error while fabricating the chip), we choose to perform single qubit gates acting on either  $S_1$  or  $S_2$  in 128 ns, slower than state-of-the-art  $^{39,40}$ , thereby decreasing the spectral overlap between the drive pulses. For the two-qubit gates, which are unaffected by the small detuning between the source qubits, we optimize gate times resulting in a 173 ns CZ gate. We perform the CNOT gates in 110 ns  $(S_1)$  and 106 ns  $(S_2)$ , and the SWAP gates in 186 ns  $(S_1)$  and 240 ns  $(S_2)$ . To ensure the emitter qubits fully decay to their ground state after a SWAP or CNOT gate, we choose a 650 ns delay between successive emission of photon pairs in our protocol. All relevant device parameters are summarized in Supplementary Note 1, Supplementary Table S1. Further details of the detection scheme and experimental setup are given in Supplementary Note 1.

#### State characterization

When generating an entangled photonic state, the emitted photons P<sub>i</sub> propagate into the common waveguide and are routed off chip into a coaxial output line. The microwave photons are then amplified and their quadratures are measured at room temperature<sup>41,42</sup>. Note that the amplification is necessary due to the low energy of microwave photons  $(\hbar\omega/k_B \sim 100 \text{ mK})$ , but adds noise, limiting the quantum efficiency  $\eta$  to around 0.25 in our state-of-the-art setup. Alternatively, one could noiselessly detect microwave photons using custom-made microwave photon detectors<sup>43-45</sup>. Here, we choose to characterize the radiation using amplification for simplicity. We characterize the emitted photonic modes  $P_i$  by recording their respective quadratures  $I_i$  and  $Q_i^{42}$ . From  $I_i$  and  $Q_i$ , we then calculate statistical moments  $\langle \hat{a}^{\dagger s} \hat{a}^t \rangle^{27}$  of the emitted photonic modes Pi. As we are interested in the statistical moments of the photonic modes when emitted from the superconducting device, we calibrate out the noise added by the amplification chain<sup>27,41</sup> as detailed in Supplementary Note 3, which makes use of the linearity of the amplification chain. Noise added during amplification therefore does ideally not affect the fidelity of the reconstructed density matrix, but rather decreases the detection efficiency  $\eta$ . As we find that the second order correlation  $\langle \hat{a}^{\dagger 2} \hat{a}^2 \rangle$  is close to zero, confirming the linearity of the detection chain (see Supplementary Note 3 for details), we truncate the Hilbert space to  $s, t \in \{0, 1\}$ , i.e., the single photon Hilbert space. To then reconstruct the density matrix of up to 4-qubit states from the integrated quadratures, we calculate joint moments  $(\hat{a}_{1}^{\dagger s} \hat{a}_{1}^{t} \hat{a}_{2}^{\dagger u} \hat{a}_{2}^{v} \hat{a}_{3}^{\dagger w} \hat{a}_{3}^{x} \hat{a}_{4}^{\dagger y} \hat{a}_{4}^{z})$ , where  $s, t, \ldots, z \in \{0, 1\}$ , of all constituent photonic qubits P<sub>i</sub> and perform maximum likelihood estimation on the extracted moments to obtain the most likely physical density matrix<sup>5,42</sup>, see Supplementary Note 4 for details.

As the number of required measurement runs to achieve a given signal-to-noise ratio  $k \propto 1/\eta^0$ , where  $\eta$  is the quantum efficiency of the detection chain, scales exponentially with the order O of the moment<sup>41</sup>, measuring joint moments of more than four photonic gubits becomes challenging. Thus, for states consisting of more than four photonic qubits, we use a two-step reconstruction process. Oubits in the generated states have at most 3 nearest neighbors. We reconstruct the density matrices of all four-qubit subsets of the generated state consisting of each qubit and its nearest neighbors. From these we efficiently reconstruct a matrix product operator representing the full density matrix, as described in ref. 28, making use of the fact that the cluster state is the unique ground state of a gapped nearest-neighbor Hamiltonian<sup>46</sup>. The algorithm iteratively finds the most likely state consistent with the reduced density matrices, see Supplementary Note 4 for details. For imperfect cluster states, the efficient tomography method introduces errors, as the reduced density matrices do not uniquely specify the global state. Therefore, the density matrices reconstructed with the efficient tomography method are only approximations to the actual density matrices. We investigate the fidelity between the reconstructed and the actual state further in Supplementary Note 4 using master equation simulations. We find that, for simulated imperfect cluster states, the fidelity between the reconstructed and the actual state drops with the size of the cluster state, indicating larger reconstruction errors in the larger reconstructed cluster states.

To illustrate the generation of the cluster states step by step, and to demonstrate the flexibility of the device in generating different states, we generate three states each consisting of six photons, each using a different number of entangling gates. The quantum circuits used to generate these three states are shown in Fig. 2a, c, e. In Fig. 2b, d, f, we show the reconstructed density matrices of these states, whose entanglement structure is illustrated in the insets. In (a, b), we perform only a single CZ entangling gate in the first emission step, followed by SWAP gates. In the other emission steps, we only apply Hadamard and SWAP gates, thus not creating entanglement. In (c. d), we add additional CHPASE and CNOT gates to create a four-qubit cluster state in a sixqubit subspace. Finally, in (e, f), we perform the full sequence of gates to generate a six-qubit cluster state. In each step we see that the addition of more entangling gates introduces additional structure to the density matrix, resulting in the intricate pattern of stripes in Fig. 2f that corresponds to a six-qubit cluster state. We choose to display the real part of the density matrix in Fig. 2b, d, f as the imaginary part (see Supplementary Note 4), which for an ideal cluster state would be zero, contains mostly noise due to dephasing and gate qubit errors and is on average about five times smaller than the real part.

We performed the  $2 \times n$ -qubit cluster state generation protocol outlined above for  $n \in \{2, 3, 4, ..., 10\}$ , resulting in cluster states of up to 20 photonic qubits. We find that the reconstructed N-photon cluster state density matrices  $\rho_{\rm Exp}$  have fidelities  $F = {\rm Tr}(\sqrt{\rho_{\rm Exp}\rho_{\rm Ideal}})^2$  of 0.84 (four qubit), 0.77 (six qubit), 0.59 (eight qubit) and 0.12 (20 qubit) to the corresponding ideal cluster state  $\rho_{\rm Ideal}$  (see Supplementary Note 4 for more details). For the four, six and eight qubit states, the fidelity therefore exceeds the threshold for genuine multipartite entanglement of 50%, i.e., the generated state cannot be written as a convex sum of bi-separable states $^{47}$ .

The density matrix of the 20 qubit cluster state, containing a total of  $2^{40} \approx 1 \times 10^{12}$  entries, is too large to display and impractical to construct as a density matrix in full, so we instead reconstruct the state entirely in the matrix product operator representation and only show the upper-left part and far off-diagonal part of the density matrix, see Fig. 3a, b for the phase and Supplementary Note 4 for the magnitude. We observe that for all cluster state density matrices for  $N=2,4,\ldots,20$ , including those not shown, elements closer to the  $|00...\rangle$  state are larger in magnitude compared to the ideal state while far off-diagonal elements are smaller in magnitude than the ideal state.

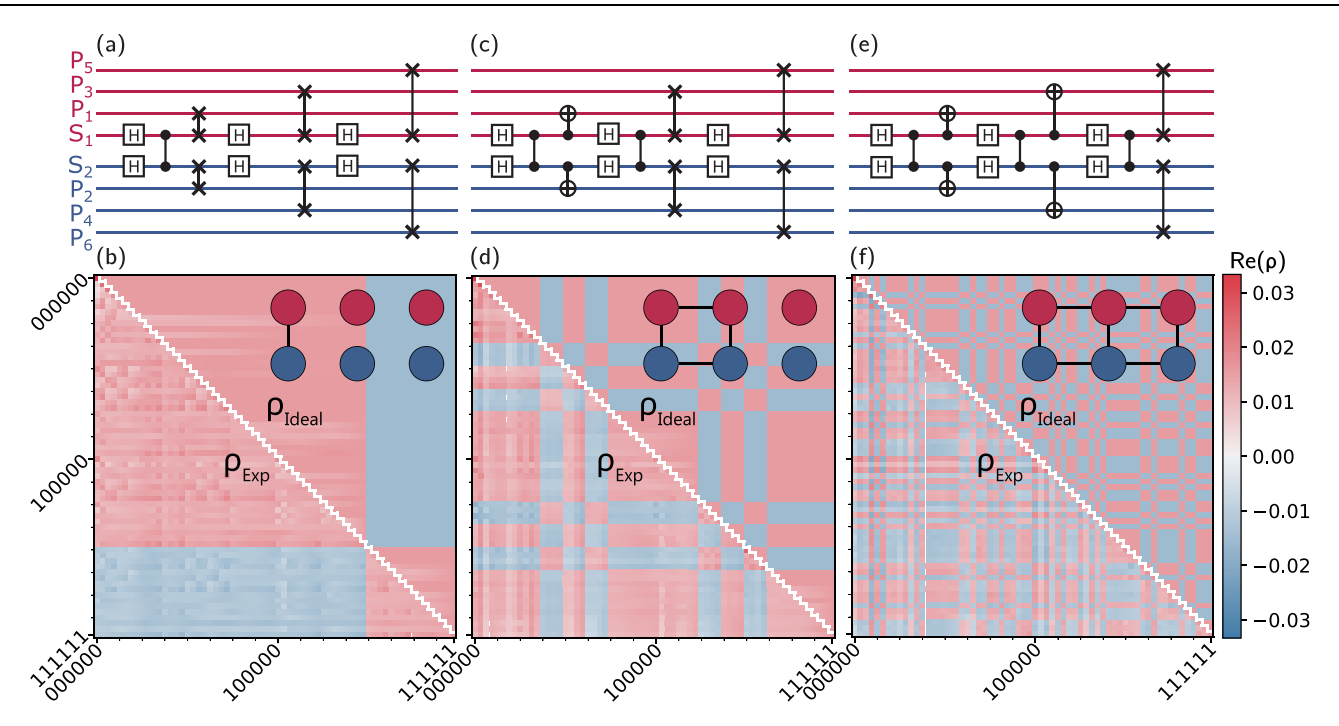


**Fig. 2** | **Step by step build-up of a six-qubit cluster state.** We prepare six photonic qubits in three separate experiments, starting with a gate sequence containing only one entangling CZ gate (a), four entangling gates (c), and finally the full sequence to generate a six-qubit cluster state (e). The resulting reconstructed density

matrices are shown in (**b**, **d**, **f**), below the corresponding gate sequences. For each density matrix an illustration of the entanglement structure is also depicted in the upper-right corner.

This is due to source qubit decay and dephasing occurring during the execution of the protocol (see Supplementary Note 4). As this dephasing causes the diagonal elements of  $Re(\rho)$  to be much larger than the off-diagonal elements, we instead plot the phase in Fig. 3a, b, which emphasizes the patterns in the phase stemming from entanglement more clearly. The patterns in Fig. 3a are not strongly affected by dephasing, as they reflect local correlations, for which the effect of dephasing is small. For the far off-diagonal elements in Fig. 3b, the patterns are also locally correct, however when comparing to the ideal state, we notice errors in relative phase between distant qubits, likely a consequence of control errors.

To further characterize the generated multi-qubit states, we estimate up to which number of qubits measurable entanglement persists across the multi-qubit state. Fidelity primarily measures how close a state is to a target state, and for states whose fidelity is less than 50% to the target state we cannot make a statement about entanglement anymore. For example, a state can be maximally entangled, but differ from the target state by single-qubit gates, rendering the fidelity to be close to 0. However, there are several metrics aimed at measuring multipartite entanglement<sup>2</sup>, and we choose to use localizable entanglement, as it is commonly used<sup>14,19</sup>. The localizable entanglement metric is also closely related to important applications like measurement-based quantum computing or error-corrected quantum communication, as obtaining the localizable entanglement metric requires measuring all but two qubits in certain bases. We thus expect that the localizable entanglement metric is indicative of the performance of generated cluster states in the context of measurement-based quantum computing or errorcorrected quantum communication.

We calculate the localizable entanglement between the first  $P_1$  and last  $P_N$  photonic qubit<sup>48,49</sup>. To do so, we project all other qubits either in the X or the Z basis and then evaluate the negativity between  $P_1$  and  $P_N$ . For a cluster state a Z projection removes the node and its bonds, while an X projection preserves the entanglement bonds<sup>49</sup>. We apply these projections to the reconstructed state in post-processing. Using X projections, we construct a path of length n = N/2, the shortest possible

distance, between  $P_1$  and  $P_N$ , while applying Z projections on all nodes outside the path; see Supplementary Note 8 for details. Figure 4a illustrates an example path for N=10. As each projection has a probabilistic outcome, for an N-qubit state, there are  $2^{N-2}$  possible outcomes for each path. For states larger than N=12 it becomes impractical to compute all such outcomes. We therefore average the obtained negativity over 1024 randomly sampled projection outcomes and obtain the localizable entanglement for each path, then average over all paths with length n=N/2. A nonzero localizable entanglement value indicates that there is measurable entanglement between  $P_1$  and  $P_N$ .

We calculate the localizable entanglement for experimentally generated and reconstructed states. However, as errors introduced by the efficient tomography method increase for larger, imperfect cluster states (see Supplementary Note 4 for details), we employ an additional complementary method to verify the results. We measure process maps of the two repeated processes (H followed by CZ and CNOT or H followed by CZ and SWAP) using process tomography. Assuming that the emission process applied does not change when photonic qubits are emitted sequentially, we repeatedly apply the extracted process maps to the initial ground state density matrix  $|gg\rangle\langle gg|$  of the source qubits to calculate the expected density matrix of the generated cluster states<sup>11,19</sup>, see Supplementary Note 6 for further details. Inferring the density matrix from the reconstructed process map assumes a repeatable process with time-independent error. In our experiment, this assumption appears to be well justified because both the microwave frequency control pulses and the system parameters are found to be stable over the microsecond timescales of individual sequences. From these density matrices we can also extract the localizable entanglement for comparison. Finally, we perform two types of master equation simulation of the state generation sequence, one taking into account only decay and dephasing errors, estimated from measured source qubit  $T_1$ ,  $T_2^*$  values, and one taking into account all errors (i.e., including coherent gate errors), see Supplementary Note 7 for further details. From these simulations, we extract the localizable entanglement from the resulting simulated density matrices. The localizable

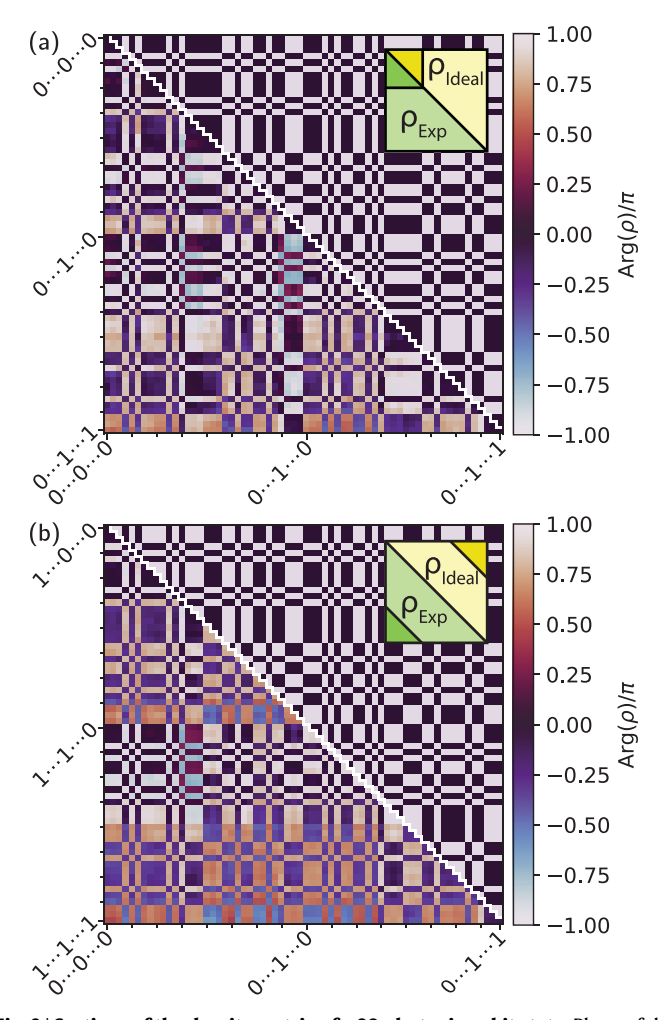


**Fig. 3** | **Sections of the density matrix of a 20 photonic qubit state.** Phase of the experimental  $\rho_{\rm Exp}$  (below diagonal) and the ideal  $\rho_{\rm Ideal}$  (above diagonal) density matrix of the 20 qubit cluster state, showing only (a) the upper-left part and b far off-diagonal part of the full density matrix. Darker colored triangles in the insets indicate the sections of the density matrix displayed.

entanglement values calculated from all above methods for states up to 20 photons in size are shown in Fig. 4. We see that the localizable entanglement gets smaller with increasing state size for all data and analyses. This is expected as larger system sizes involve longer gate sequences and therefore more decoherence and gate errors. The simulations including only decay and dephasing have larger localizable entanglement than those taking into account all errors, indicating that coherent gate errors make a significant contribution to the overall error in state generation. The localizable entanglement extracted from process maps agrees well with the simulation including all errors, while the experimentally generated and reconstructed density matrices for N>8 yield localizable entanglement values significantly below that of the process maps and simulations. This is most likely due to errors introduced by the efficient tomography method. To verify this, we apply the efficient tomography method to density matrices obtained from master equation simulations and observe a reduction in the extracted localizable entanglement and fidelity of the reconstructed density matrices compared to the simulated density matrices, which do not require reconstruction, see Supplementary Note 4 for details. The efficient tomography method thus, at least for the simulated states, results in a conservative estimate of the localizable entanglement. In addition, both the results from process tomography as well as simulations indicate a larger localizable entanglement. Using the most conservative localizable entanglement estimate obtained with the

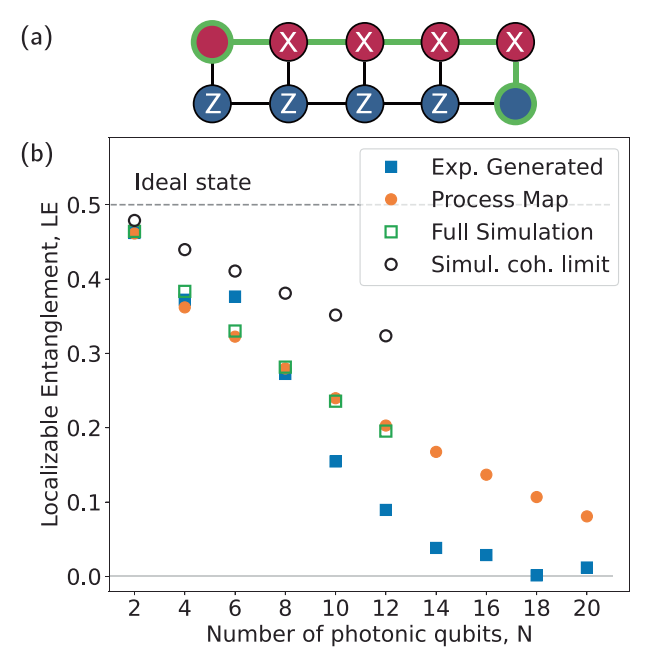


**Fig. 4** | **Quantifying entanglement of the generated states. a** Schematic illustrating the chosen localizable entanglement metric for a 10 photonic qubit state. Qubits are projected into either the X or the Z bases, as indicated, then localizable entanglement is calculated for the two corner qubits (green edges). b Localizable entanglement as a function of number of generated photonic qubits  $N=2\times n$ , as measured by matrix product operator tomography of the experimentally generated states (exp. generated, blue, solid squares), as estimated from process maps (orange, solid circles), and as obtained by master equation simulations taking into account all errors (green, empty squares) and only decoherence (simul. coh. limit (simulated coherence limit), black, open circles), and the localizable entanglement of the ideal state (gray, dashed line). Shown is the mean over all possible paths of length n.

three reconstruction methods, we see that the localizable entanglement is nonzero for states comprising up to 16 qubits, and drops to near-zero for the measured 18- and 20-qubit states. On the other hand, the process tomography does not suffer from the limitations of the efficient tomography methods for reconstructing large and imperfect cluster state, and predicts that entanglement should persist for even larger states.

From the analysis of process maps and master equation simulations, we conclude that the ultimate size of the states we can generate is limited both by the fidelity of our single and two-qubit gates and from decoherence during the pulse sequence. Qubit drive-line crosstalk is likely primarily responsible for the single qubit gate error and crosstalk cancellation should alleviate this. Further optimization of the coupler design and qubit frequencies and fine-tuning of the gate parameters may be feasible to increase two-qubit gate (in particular, the CZ gate) fidelities, which we, using simulations, estimate to currently be around 97%, towards the state-of-the-art performance for similar tunable coupler designs<sup>50</sup>. Extending qubit coherence times from 22  $\mu$ s (S<sub>1</sub>) and 23  $\mu$ s (S<sub>2</sub>) towards the state of the art, which is more than an order of magnitude longer<sup>51</sup>, will reduce the decoherencerelated error that we observe in the largest states generated. This will permit the utilization of significantly longer gate sequences to generate larger 2D entangled states.

# **Discussion**

In conclusion, we demonstrate deterministic generation of cluster states consisting of up to 20 photons entangled in two dimensions with nonzero localizable entanglement persisting across 20 constituent photons. We extract a fidelity of 84%, 77% and 59% for four-,

six- and eight-photon 2D entangled states, respectively. We employ efficient tomography techniques to reconstruct the density matrix of states whose size precludes the use of direct tomography. These techniques are not specific to superconducting circuits and could be applied in the context of any physical platform. We perform process tomography on the constituent parts of the experimental gate sequence and master equation simulations to extract the expected quality of generated states.

With the previously outlined improvements to our device, it should be feasible to significantly extend the duration of our protocol to generate larger cluster states. In addition, our architecture is scalable by fabricating additional stationary qubits. Two-qubit gates could be alternated such that all such gates necessary for an  $m \times n$  sized 2D-entangled cluster state could be performed in no more than two sequential steps for any number m of source qubits, making the scaling of gate sequence time in this protocol extremely attractive.

The device architecture is in principle capable of creating states such as repeater states or tree graph states, which are relevant for a variety of quantum communication protocols<sup>52–54</sup>. The architecture also supports other encoding schemes for photonic qubits, such as time-bin encoding<sup>55</sup>. Time-bin encoded qubits allow for the detection of photon loss, and are thus required in many quantum communication protocols<sup>52–54</sup>. As emitting in the time-bin basis requires approximately twice the number of two-qubit gates, further improving gate fidelities and coherence times is crucial for using the device in the context of quantum communication.

Addition of either a quantum memory or greater connectivity between qubits could allow generation of higher-dimensional states. The prospect to generate a wide variety of entangled photonic states at a significantly larger scale opens up exciting possibilities for using such states for measurement-based quantum computing, metrology or quantum communication protocols in the context of the fast-growing field of waveguide QED.

#### Data availability

The data generated in this study have been deposited in the ETH Zurich repository for research data and are publicly available at the following url: https://doi.org/10.3929/ethz-b-000735974.

#### Code availability

The code used for data analysis is available from the corresponding authors upon request.

# References

- Bennett, C. H. & DiVincenzo, D. P. Quantum information and computation. Nature 404, 247–255 (2000).
- Horodecki, R., Horodecki, P., Horodecki, M. & Horodecki, K. Quantum entanglement. Rev. Mod. Phys. 81, 865–942 (2009).
- Raussendorf, R. & Briegel, H. J. A one-way quantum computer. *Phys. Rev. Lett.* 86, 5188–5191 (2001).
- Raussendorf, R., Browne, D. E. & Briegel, H. J. Measurement-based quantum computation on cluster states. *Phys. Rev. A* 68, 022312 (2003).
- Ferreira, V. S., Kim, G., Butler, A., Pichler, H. & Painter, O. Deterministic generation of multidimensional photonic cluster states with a single quantum emitter. *Nat. Phys.* 20, 865–870 (2024).
- Cao, S. et al. Generation of genuine entanglement up to 51 superconducting qubits. Nature 619, 738–742 (2023).
- 7. Lanyon, B. P. et al. Measurement-based quantum computation with trapped ions. *Phys. Rev. Lett.* **111**, 210501 (2013).
- 8. Friis, N. et al. Observation of entangled states of a fully controlled 20-qubit system. *Phys. Rev. X* **8**, 021012 (2018).
- 9. Wang, Y., Li, Y., Yin, Z.-q & Zeng, B. 16-qubit IBM universal quantum computer can be fully entangled. *npj Quantum Inf.* **4**, 46 (2018).

- 10. Wei, K. X. et al. Verifying multipartite entangled Greenberger-Horne-Zeilinger states via multiple quantum coherences. *Phys. Rev.* A **101**, 032343 (2020).
- Schwartz, I. et al. Deterministic generation of a cluster state of entangled photons. Science 354, 434–437 (2016).
- Larsen, M. V., Guo, X., Breum, C. R., Neergaard-Nielsen, J. S. & Andersen, U. L. Deterministic generation of a two-dimensional cluster state. Science 366, 369–372 (2019).
- Asavanant, W. et al. Generation of time-domain-multiplexed twodimensional cluster state. Science 366, 373–376 (2019).
- 14. Istrati, D. et al. Sequential generation of linear cluster states from a single photon emitter. *Nat. Commun.* 11, 1–8 (2020).
- 15. Roh, C., Gwak, G., Yoon, Y. & Ra, Y. Generation of three-dimensional cluster entangled state. *Nat. Photonics* **19**, 526–532 (2023).
- Foss-Feig, M. et al. Entanglement from tensor networks on a trapped-ion quantum computer. Phys. Rev. Lett. 128, 150504 (2022).
- Schön, C., Solano, E., Verstraete, F., Cirac, J. & Wolf, M. Sequential generation of entangled multiqubit states. *Phys. Rev. Lett.* 95, 110503 (2005).
- Liu, C., Barnes, E. & Economou, S. Proposal for generating complex microwave graph states using superconducting circuits. Preprint at https://arxiv.org/abs/2201.00836 (2022).
- Besse, J.-C. et al. Realizing a deterministic source of multipartiteentangled photonic qubits. Nat. Commun. 11, 4877 (2020).
- Thomas, P., Ruscio, L., Morin, O. & Rempe, G. Efficient generation of entangled multiphoton graph states from a single atom. *Nature* 608, 677–681 (2022).
- Thomas, P., Ruscio, L., Morin, O. & Rempe, G. Fusion of deterministically generated photonic graph states. *Nature* 629, 567–572 (2024).
- 22. Kjaergaard, M. et al. Superconducting qubits: current state of play. *Annu. Rev. Condens. Matter Phys.* **11**, 369–395 (2020).
- Blais, A., Grimsmo, A. L., Girvin, S. M. & Wallraff, A. Circuit quantum electrodynamics. Rev. Mod. Phys. 93, 025005 (2021).
- 24. Wallraff, A. et al. Strong coupling of a single photon to a super-conducting qubit using circuit quantum electrodynamics. *Nature* **431**, 162–167 (2004).
- 25. Houck, A. A. et al. Generating single microwave photons in a circuit. *Nature* **449**, 328–331 (2007).
- Collodo, M. C. et al. Implementation of conditional phase gates based on tunable ZZ interactions. *Phys. Rev. Lett.* 125, 240502 (2020).
- 27. Eichler, C. et al. Experimental state tomography of itinerant single microwave photons. *Phys. Rev. Lett.* **106**, 220503–4 (2011).
- 28. Baumgratz, T., Nüßeler, A., Cramer, M. & Plenio, M. B. A scalable maximum likelihood method for quantum state tomography. *New J. Phys.* **15**, 125004 (2013).
- Kurpiers, P., Walter, T., Magnard, P., Salathe, Y. & Wallraff, A. Characterizing the attenuation of coaxial and rectangular microwave-frequency waveguides at cryogenic temperatures. *EPJ Quantum Technol.* 4, 8 (2017).
- Naik, R. K. et al. Random access quantum information processors using multimode circuit quantum electrodynamics. *Nat. Commun.* 8, 1904 (2017).
- 31. Matanin, A. R. et al. Toward highly efficient multimode super-conducting quantum memory. *Phys. Rev. Appl.* **19**, 034011 (2023).
- 32. Pichler, H. & Zoller, P. Photonic circuits with time delays and quantum feedback. *Phys. Rev. Lett.* **116**, 093601 (2016).
- 33. Koch, J. et al. Charge-insensitive qubit design derived from the Cooper pair box. *Phys. Rev. A* **76**, 042319 (2007).
- Mundada, P., Zhang, G., Hazard, T. & Houck, A. Suppression of qubit crosstalk in a tunable coupling superconducting circuit. *Phys. Rev. Appl.* 12, 054023 (2019).

- 35. Reagor, M. et al. Demonstration of universal parametric entangling gates on a multi-gubit lattice. *Sci. Adv.* **4**, eaao3603 (2018).
- Reuer, K. et al. Realization of a universal quantum gate set for itinerant microwave photons. Phys. Rev. X 12, 011008 (2022).
- Strauch, F. W. et al. Quantum logic gates for coupled superconducting phase qubits. Phys. Rev. Lett. 91, 167005 (2003).
- 38. DiCarlo, L. et al. Preparation and measurement of three-qubit entanglement in a superconducting circuit. *Nature* **467**, 574–578 (2010).
- 39. Werninghaus, M. et al. Leakage reduction in fast superconducting qubit gates via optimal control. *npj Quantum Inf.* **7**, 14 (2021).
- Lazăr, S. et al. Calibration of drive nonlinearity for arbitrary-angle single-qubit gates using error amplification. *Phys. Rev. Appl.* 20, 024036 (2023).
- da Silva, M. P., Bozyigit, D., Wallraff, A. & Blais, A. Schemes for the observation of photon correlation functions in circuit QED with linear detectors. *Phys. Rev. A* 82, 043804 (2010).
- 42. Eichler, C., Bozyigit, D. & Wallraff, A. Characterizing quantum microwave radiation and its entanglement with superconducting qubits using linear detectors. *Phys. Rev. A* **86**, 032106 (2012).
- Besse, J.-C. et al. Single-shot quantum non-demolition detection of individual itinerant microwave photons. *Phys. Rev. X* 8, 021003 (2018).
- 44. Kono, S., Koshino, K., Tabuchi, Y., Noguchi, A. & Nakamura, Y. Quantum non-demolition detection of an itinerant microwave photon. *Nat. Phys.* **14**, 546–549 (2018).
- Lescanne, R. et al. Irreversible qubit-photon coupling for the detection of itinerant microwave photons. *Phys. Rev. X* 10, 021038 (2020).
- 46. Briegel, H. J. & Raussendorf, R. Persistent entanglement in arrays of interacting particles. *Phys. Rev. Lett.* **86**, 910–913 (2001).
- Gühne, O. & Tóth, G. Entanglement detection. *Phys. Rep.* 474, 1–75 (2009).
- 48. Verstraete, F., Popp, M. & Cirac, J. I. Entanglement versus correlations in spin systems. *Phys. Rev. Lett.* **92**, 027901 (2004).
- 49. Hein, M. et al. Entanglement in graph states and its applications. Preprint at https://arxiv.org/abs/quant-ph/0602096 (2006).
- 50. Marxer, F. et al. Long-distance transmon coupler with CZ-Gate fidelity above 99.8 %. *PRX Quantum* **4**, 010314 (2023).
- 51. Wang, C. et al. Towards practical quantum computers: transmon qubit with a lifetime approaching 0.5 milliseconds. *npj Quantum Inf.* **8**, 3 (2022).
- 52. Buterakos, D., Barnes, E. & Economou, S. E. Deterministic generation of all-photonic quantum repeaters from solid-state emitters. *Phys. Rev. X* **7**, 041023 (2017).
- Borregaard, J. et al. One-way quantum repeater based on neardeterministic photon-emitter interfaces. *Phys. Rev. X* 10, 021071 (2020).
- Bell, T. J., Pettersson, L. A. & Paesani, S. Optimizing graph codes for measurement-based loss tolerance. *PRX Quantum* 4, 020328 (2023).
- 55. Kurpiers, P. et al. Quantum communication with time-bin encoded microwave photons. *Phys. Rev. Appl.* **12**, 044067 (2019).

#### **Acknowledgements**

We are grateful for the contributions of Alexander Ferk to the experimental setup and Graham J. Norris for photomask fabrication. This work was supported by the Swiss National Science Foundation (SNSF) through the project "Quantum Photonics with Microwaves in

Superconducting Circuits" (Grant No. 200021\_184686), by the European Research Council (ERC) through the project "Superconducting Quantum Network" (SuperQuNet) and by ETH Zurich. Support is also acknowledged from the U.S. Department of Energy, Office of Science, National Quantum Information Science Research Centers, Quantum Systems Accelerator. Additional support is acknowledged from the Ministére de l'Économie et de l'Innovation du Québec, NSERC, and the Canada First Research Excellence Fund. D.M. acknowledges financial support from the Novo Nordisk Foundation under grant numbers NF22OC0071934 and NNF20OC0059939.

## **Author contributions**

J.O. and K.R. designed the device. A.F., D.C.Z. and J.-C.B. fabricated the device. J.O. and K.R. prepared the experimental setup. J.O., K.R., A.G., X.D. and A.H. characterized and calibrated the device and the experimental setup. J.O., K.R., A.G., X.D. and A.H. carried out the experiments and analyzed the data, with support from D.M. and C.H. M.M. performed the master equation simulations. J.O. and K.R. wrote the manuscript with input from all co-authors. J.-C.B., A.B., C.E. and A.W. supervised the work.

#### **Competing interests**

The authors declare no competing interests.

## **Additional information**

**Supplementary information** The online version contains supplementary material available at https://doi.org/10.1038/s41467-025-60472-3.

**Correspondence** and requests for materials should be addressed to James O'Sullivan, Kevin Reuer or Andreas Wallraff.

**Peer review information** *Nature Communications* thanks the anonymous reviewer(s) for their contribution to the peer review of this work. A peer review file is available.

**Reprints and permissions information** is available at http://www.nature.com/reprints

**Publisher's note** Springer Nature remains neutral with regard to jurisdictional claims in published maps and institutional affiliations.

Open Access This article is licensed under a Creative Commons Attribution-NonCommercial-NoDerivatives 4.0 International License, which permits any non-commercial use, sharing, distribution and reproduction in any medium or format, as long as you give appropriate credit to the original author(s) and the source, provide a link to the Creative Commons licence, and indicate if you modified the licensed material. You do not have permission under this licence to share adapted material derived from this article or parts of it. The images or other third party material in this article are included in the article's Creative Commons licence, unless indicated otherwise in a credit line to the material. If material is not included in the article's Creative Commons licence and your intended use is not permitted by statutory regulation or exceeds the permitted use, you will need to obtain permission directly from the copyright holder. To view a copy of this licence, visit <a href="https://creativecommons.org/licenses/by-nc-nd/4.0/">https://creativecommons.org/licenses/by-nc-nd/4.0/</a>.

© The Author(s) 2025